19

Monitoring Natural Hazards in Protected Lands Using Interferometric Synthetic Aperture Radar

Zhong Lu, Daniel Dzurisin, and Hyung-Sup Jung

CONTENTS

19.1 Introduction

Natural hazards in protected lands frequently result in damage to or loss of lives, livelihoods, structures, or ecosystem productivity. Often, natural hazards occur in remote areas of protected lands or impact such large areas that *in situ* measurements are not feasible, accurate, or timely enough for monitoring or early warning. Satellite interferometric synthetic aperture radar (InSAR) provides an all-weather imaging capability for measuring ground-surface deformation with centimeter-to-subcentimeter precision and inferring changes in landscape characteristics over a large region. With its global coverage and all-weather imaging capability, InSAR is an important remote sensing technique for measuring ground-surface deformation of various natural hazards and the associated landscape changes. The spatial distribution of surface deformation data, derived from InSAR imagery, enables the construction of detailed numerical models to enhance the study of physical processes of natural hazards. This chapter (a) introduces the basics of InSAR for deformation mapping and landscape change detection, (b) discusses state-of-the-art technical issues in InSAR processing and interpretation, and (c) showcases the application of InSAR to the study of volcano, earthquake, landslide, and glacier movement and the mapping of high-resolution digital elevation model and fire progression with InSAR imagery over protected lands.

19.2 Principles of Interferometric Synthetic Aperture Radar

19.2.1 Imaging Radar

Radar is an acronym for radio detection and ranging, which hints at some of the technique's uses and capabilities (Levanon, 1988). Radar operates by broadcasting a pulse of electromagnetic energy into space. If the pulse encounters an object, some of the energy is redirected back to the radar. The same antenna can be used to transmit the initial pulse and receive the return signal. Precise timing of the delay between the initial and return signals allows determination of the distance from radar to object, and the Doppler frequency shift between the two signals is a measure of the object's velocity relative to the radar. Thus, radar can be used to detect and measure the velocity of things such as aircraft or highway vehicles—two common uses of Doppler radar. But radar's capabilities extend far beyond air traffic control and law enforcement.

Imaging radar systems operate on the same principles but have additional capability to distinguish among return signals from individual resolution elements within a target footprint. This enables processing of resulting data

into an image of the target area, which contains information about topography and radar reflective properties of the surface. The resolution of real-aperture imaging radar systems depends on, among other factors, the size of the antenna (bigger is better), which, for practical reasons, is limited to a few meters or decimeters. This limitation can be overcome, however, by creating a much larger "synthetic" radar antenna.

19.2.2 Synthetic Aperture Radar

Synthetic aperture radar (SAR) is an advanced radar system that utilizes image processing techniques to synthesize a large virtual antenna, which provides much higher spatial resolution than is practical using a real-aperture radar. Because SAR actively transmits and receives signals backscattered from the target area, and because radar wavelengths are mostly unaffected by weather clouds, SAR can operate effectively during day and night under most weather conditions. Using a sophisticated image processing technique, called SAR processing (Bamler and Hartl, 1998; Curlander and McDonough, 1991; Henderson and Lewis, 1998), both intensity and phase of the reflected (or backscattered) signal of each ground resolution element (a few meters to tens of meters) can be calculated in the form of a complex-valued SAR image representing the reflectivity of the ground surface. The intensity of the SAR image (Figure 19.1a) is controlled primarily by terrain slope, surface roughness, and dielectric constants, whereas the phase of the SAR image (Figure 19.1b) is controlled primarily by the distance from the satellite antenna to ground targets, the atmospheric delays, and the interaction of electromagnetic waves with the ground surface.

19.2.3 Basics of Interferometric SAR

InSAR is formed by interfering signals from two spatially or temporally separated antennas. The term "interferometry" draws its meaning from two root words: interfere and measure. The interaction of electromagnetic waves, referred to as interference, is used to measure precise distances and angles. Interference of electromagnetic waves that are transmitted and received by SAR, an advanced imaging radar instrument, is called InSAR. Very simply, InSAR involves the use of two or more SAR images of the same area to extract the land surface topography and its deformation patterns.

For InSAR purposes, the spatial separation between two SAR antennas, or between two vantage points of the same SAR antenna, is called the baseline. The two antennas may be mounted on a single platform for simultaneous interferometry, the usual implementation for aircraft and spaceborne systems such as Topographic SAR (TOPSAR) and Shuttle Radar Topography Mission (SRTM) systems (Farr et al., 2007; Zebker et al., 1992). Alternatively, InSAR images can be formed by using a single antenna on an airborne or spaceborne platform in nearly identical repeating flight lines or orbits for

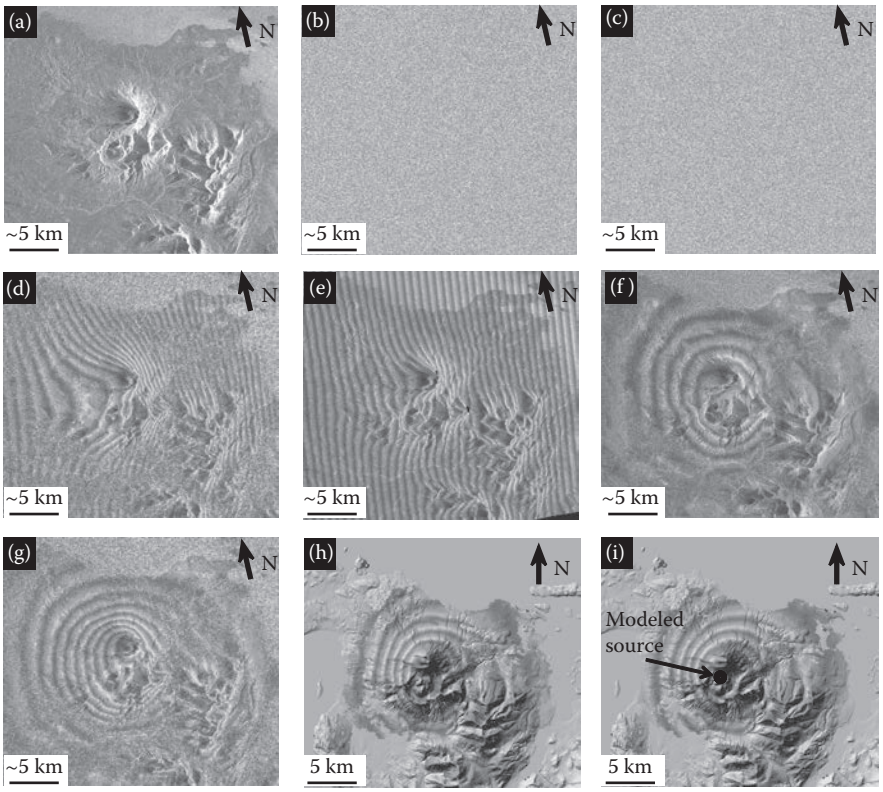

FIGURE 19.1
(**See color insert.**) (a) The amplitude component of an SLC SAR image acquired on October 4, 1995, by ERS-1 satellite over Peulik Volcano, Alaska. (b) The phase component of the SAR image acquired on October 4, 1995, corresponding to the amplitude image in (a). (c) The phase of an SLC SAR image acquired on October 9, 1997, by ERS-2 satellite over Peulik Volcano, Alaska. The amplitude image is similar to that in (a) and therefore is not shown. (d) An original interferogram formed by differencing the phase values of two coregistered SAR images (b and c). The resulting interferogram contains fringes produced by the differing viewing geometries, topography, any atmospheric delays, surface deformation, and noise. (e) An interferogram simulated to represent the topographic contribution in the original interferogram (d). The perpendicular component of the InSAR baseline is 35 m. (f) A topography-removed interferogram produced by subtracting the interferogram in (e) from the original interferogram in (d). The resulting interferogram contains fringes produced by surface deformation, any atmospheric delays, and noise. (g) A flattened interferogram that was produced by removing the effect of an ellipsoidal earth surface from the original interferogram (d). The resulting interferogram contains fringes produced by topography, surface deformation, any atmospheric delays, and noise. (h) A georeferenced topography-removed interferogram (f) overlaid on a shaded relief image produced from a DEM. The concentric pattern indicates ~17 cm of uplift centered on the southwest flank of Peulik Volcano, Alaska, which occurred during an aseismic inflation episode (Lu et al., 2002). (i) A modeled interferogram produced using a best-fit inflationary point source at ~6.5- km depth with a volume change of ~0.043 km^3 on the observed deformation image in (g). Each interferometric fringe (full-color cycle) represents 360° of phase change (or 2.83 cm of range change between the ground and the satellite). Areas of loss of radar coherence are uncolored in (h) and (i).

repeat-pass interferometry (Gray and Farris-Manning, 1993; Massonnet and Feigl, 1998). In this case, even though successive observations of the target area are separated in time, the observations will be highly correlated if the backscattering properties of the surface have not changed in the interim. In this way, InSAR is capable of measuring ground-surface deformation with subcentimeter precision for X-band and C-band sensors (wavelength $\lambda = 2–8$ cm), or few-centimeter precision for L-band sensors ($\lambda = 15–30$ cm), in both cases at a spatial resolution of tens of meters over an image swath (width) of a few tens of hundreds of kilometers. This is the typical implementation for spaceborne sensors, including European Space Agency (ESA) European Remote-sensing Satellite 1 (ERS-1) (operated 1991–2000, C-band, $\lambda = 5.66$ cm), Japan Aerospace Exploration Agency (JAXA) Japanese Earth Resources Satellite 1 (JERS-1) (1992–1998, L-band, $\lambda = 23.5$ cm), ESA European Remote-sensing Satellite 2 (ERS-2) (1995–present, C-band, $\lambda = 5.66$ cm), Canadian Space Agency (CSA) Canadian Radar Satellite 1 (RADARSAT-1) (1995–present, C-band, $\lambda = 5.66$ cm), ESA European Environmental Satellite (Envisat) (2002–present, C-band, $\lambda = 5.63$ cm), JAXA Japanese Advanced Land Observing Satellite (ALOS) (January 2006–present, L-band, $\lambda = 23.6$ cm), CSA RADARSAT-2 (2007–present, C-band, $\lambda = 5.55$ cm), German Aerospace Agency (DLR) TerraSAR-X (2007–present, X-band, $\lambda = 3.1$ cm), Italian COSMO-SkyMed satellite constellation (2007–present, X-band, $\lambda = 3.1$ cm) and German Aerospace Agency (DLR) TerraSAR add-on for Digital Elevation Measurements (TanDEM-X) (2010–present, X-band, $\lambda = 3.1$ cm).

The generation of an interferogram requires two single-look-complex (SLC) SAR images. Neglecting phase shifts induced by the transmitting/receiving antenna and SAR processing algorithms, the phase value of a pixel in an SLC SAR image (Figure 19.1b) can be represented as

$$\phi_1 = -\frac{4\pi}{\lambda} r_1 + \varepsilon_1 \tag{19.1}$$

where r_1 (a deterministic variable) is the apparent range distance (including possible atmospheric delay) from the antenna to the ground target, λ is the wavelength of radar, and ε_1 is the sum of phase shift due to the interaction between the incident radar wave and scatterers within the resolution cell. Because the backscattering phase (ε_1) is a stochastic (randomly distributed, unknown) variable, the phase value (ϕ_1) in a single SAR image cannot be used to calculate the range (r_1) and is of no practical use. However, a second SLC SAR image (with the phase image shown in Figure 19.1c) could be obtained over the same area at a different time with a phase value of

$$\phi_2 = -\frac{4\pi}{\lambda} r_2 + \varepsilon_2 \tag{19.2}$$

Note that phase values in the second SAR image (Figure 19.1c) cannot provide range information (r_2) either, due to the stochastic nature of the backscattering phase ε_2.

An interferogram (Figure 19.1d) is created by coregistering two SAR images and differencing the corresponding phase values of the two SAR images (Figure 19.1b and c) on a pixel-by-pixel basis. The phase value of the resulting interferogram (Figure 19.1d) is

$$\phi = \phi_1 - \phi_2 = -\frac{4\pi(r_1 - r_2)}{\lambda} + (\varepsilon_1 - \varepsilon_2) \tag{19.3}$$

The fundamental assumption in repeat-pass InSAR is that the scattering characteristics of the ground surface remain undisturbed. The degree of changes in backscattering characteristics can be quantified by the interferometric coherence, which is discussed further in a later section. Assuming that the interactions between the radar waves and scatterers remain the same when the two SAR images were acquired (i.e., $\varepsilon_1 = \varepsilon_2$), the interferometric phase value can be expressed as

$$\phi = -\frac{4\pi(r_1 - r_2)}{\lambda} \tag{19.4}$$

Nominal values for the range difference ($r_1 - r_2$) extend from a few meters to several hundred meters. The SAR wavelength (λ) is of the order of several centimeters. Because the measured interferometric phase value (ϕ) is modulated by 2π, ranging from $-\pi$ to π, there is an ambiguity of many cycles (i.e., numerous 2π values) in the interferometric phase value. Therefore, the phase value of a single pixel in an interferogram is of no practical use. However, the change in range difference, $\delta(r_1 - r_2)$, between two neighboring pixels that are a few meters apart is normally much smaller than the SAR wavelength. So the phase difference between two nearby pixels, $\delta\phi$, can be used to infer the range distance difference ($r_1 - r_2$) to a subwavelength precision. This explains how InSAR uses the phase difference to infer the change in range distance to an accuracy of centimeters or millimeters.

The phase (or range distance difference) in the original interferogram represented by Equation 19.4 and exemplified by Figure 19.1d contains contributions from both the topography and any possible ground-surface deformation. In order to derive a deformation map, the topographic contribution needs to be removed from the original interferogram (Figure 19.1d). The most common procedure is to use an existing digital elevation model (DEM) and the InSAR imaging geometry to produce a synthetic interferogram and subtract it from the interferogram to be studied (e.g., Massonnet and Feigl, 1998; Rosen et al., 2000). This is the so-called two-pass InSAR. Alternatively, the synthetic interferogram that represents the topographic contribution can come from a different interferogram of the same area. The procedures are

then called three-pass or four-pass InSAR (Zebker et al., 1994). As the two-pass InSAR method is commonly used in deformation mapping, a brief explanation of how to simulate the topographic effect based on an existing DEM follows.

Two steps are required to simulate a topography-only interferogram based on a DEM. First, the DEM needs to be resampled to project heights from a map coordinate into the appropriate radar geometry via geometric simulation of the imaging process. The InSAR imaging geometry is shown in Figure 19.2. The InSAR system acquires two images of the same scene with SAR platforms located at A_1 and A_2. The baseline, defined as the vector from A_1 to A_2, has a length B and is tilted with respect to the horizontal by an angle α. The slant range r from the SAR to a ground target T with an elevation value h is linearly related to the measured phase values in the SAR

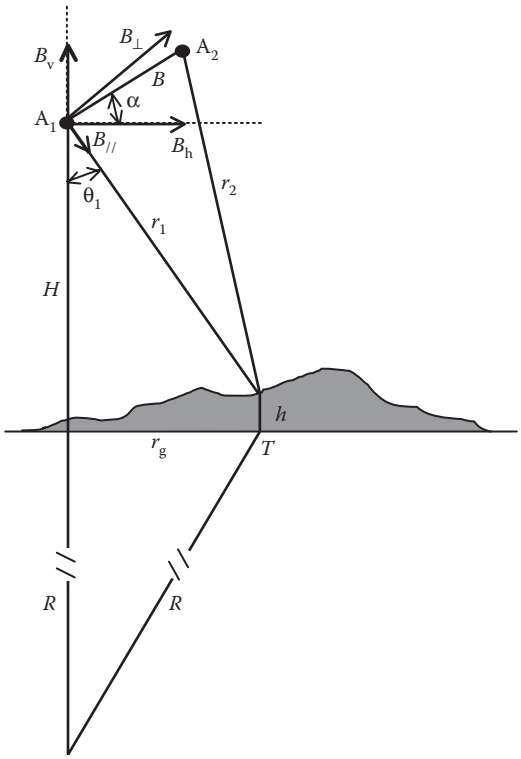

FIGURE 19.2
InSAR imaging geometry. The InSAR system acquires two images of the same scene with SARs located at A_1 and A_2. The spatial distance between A_1 and A_2 is called baseline, which has a length B and is tilted with respect to the horizontal by an angle α. The baseline B can be expressed by a pair of horizontal (B_h) and vertical (B_v) components, or a pair of parallel ($B_{//}$) and perpendicular ($B_\perp$) components. The range distances from the SARs to a ground target T with elevation h are r_1 and r_2, respectively. The look angle from A_1 to the ground point T is θ_1.

images by Equations 19.1 and 19.2. The look angle from A_1 to the ground point T is θ_1. For each ground resolution cell at ground range r_g with elevation h, the slant range value (r_1) should satisfy

$$r_1 = \sqrt{(H+R)^2 + (R+h)^2 - 2(H+R)(R+h)\cos\left(\frac{r_g}{R}\right)} \tag{19.5}$$

where H is the satellite altitude above a reference Earth surface, which is assumed to be a sphere with radius R. The radar slant range and azimuth coordinates are calculated for each point in the DEM. This set of coordinates forms a nonuniformly sampled grid in the SAR coordinate space. The DEM height data are then resampled into a uniform grid in the radar coordinates using the values over the nonuniform grid.

Second, the precise look angle from A_1 to ground target T at the ground range r_g (slant range r_1) and elevation h is calculated by

$$\theta_1 = \arccos\left[\frac{(H+R)^2 + r_1^2 - (R+h)^2}{2(H+R)r_1}\right] \tag{19.6}$$

By knowing θ_1, the interferometric phase value due to the topographic effect at target T can be calculated by

$$\phi_{dem} = -\frac{4\pi}{\lambda}(r_1 - r_2) = \frac{4\pi}{\lambda}\left(\sqrt{r_1^2 - 2(B_h \sin\theta_1 - B_v \cos\theta_1)r_1 + B^2} - r_1\right) \tag{19.7}$$

where B_h and B_v are horizontal and vertical components of the baseline B (Figure 19.1).

Figure 19.1e shows the simulated topographic effect in the interferogram in Figure 19.1d, using an existing DEM and the InSAR imaging geometry for the interferometric pair (Figure 19.2). Removing the topographic effects (Figure 19.1e) from the original interferogram (Figure 19.1d) results in an interferogram containing the ground-surface deformation during the time duration and the measurement noise (Figure 19.1f) with the phase value given as

$$\phi_{def} = \phi - \phi_{dem} \tag{19.8}$$

In practice, an ellipsoidal Earth surface, characterized by its major axis, e_{maj}, and minor axis, e_{min}, is used to replace the spherical Earth. The radius of the Earth over the imaged area is then

$$R = \sqrt{(e_{min}\sin\beta)^2 + (e_{maj}\cos\beta)^2} \tag{19.9}$$

where β is the latitude of the center of the imaged region.

If h is taken as zero, the procedure outlined in Equations 19.5 through 19.9 will remove the effect of an ellipsoidal Earth surface on the interferogram. This results in a flattened interferogram, where its phase value can be mathematically approximated as

$$\phi_{\text{flat}} = -\frac{4\pi}{\lambda}\frac{B\cos(\theta_1 - \alpha)}{r_1 \sin\theta_1}h + \phi_{\text{def}} = -\frac{4\pi}{\lambda}\frac{B_\perp}{H\tan\theta_1}h + \phi_{\text{def}} \qquad (19.10)$$

where $B_\perp$ is the perpendicular component of the baseline with respect to the incidence angle θ_1 (Figure 19.2). Removing the effect of an ellipsoidal Earth surface on the original interferogram (Figure 19.1d) will result in a flattened interferogram (Figure 19.1g).

If ϕ_{def} is negligible in Equation 19.10, the phase value in Equation 19.10 can be used to calculate height h. This explains how InSAR can be used to produce an accurate, high-resolution DEM over a large region such as the SRTM DEM (Farr et al., 2007). For the ERS-1/-2 satellites, H is about 800 km, θ_1 is about 23° ± 3°, λ is 5.66 cm, and $B_\perp$ should be less than 1100 m for a coherent interferogram. Therefore, Equation 19.10 can be approximated as

$$\phi_{\text{flat}} \approx -\frac{2\pi}{9600}B_\perp h + \phi_{\text{def}} \qquad (19.11)$$

For an interferogram with $B_\perp$ of 100 m, 1 m of topographic relief produces a phase value of about 4°. However, producing the same phase value requires only 0.3 mm of surface deformation. Therefore, it is evident that the interferogram phase value can be much more sensitive to changes in topography (i.e., the surface deformation ϕ_{def}) than to the topography itself (i.e., h). That explains why repeat-pass InSAR is capable of detecting surface deformation at a theoretical accuracy of subcentimeters.

In the two-pass InSAR deformation mapping, errors in the DEM can be mapped into deformation measurement. This is characterized by a term called the "altitude of ambiguity," which is the amount of topographic error required to generate one interferometric fringe in a topography-removed interferogram (Massonnet and Feigl, 1998). Because the altitude of ambiguity is inversely proportional to the baseline $B_\perp$, interferometric pairs with smaller baselines are better suited for deformation analysis.

The final procedure in two-pass InSAR is to rectify the SAR images and interferograms into a map coordinate, which is a backward transformation of Equation 19.5. The geo-referenced interferogram (Figure 19.1h) and derived products can be readily overlaid with other data layers to enhance the utility of the interferograms and facilitate data interpretation. Figure 19.1h shows six concentric fringes that represent about 17 cm of range decrease (mostly uplift) centered on the southwest flank of Mount Peulik, Alaska. The volcano inflated aseismically from October 1996 to September 1998, a period that included an intense earthquake swarm that started in May 1998 over 30 km northwest of Peulik Volcano (Lu et al., 2002).

In-depth description of InSAR processing can be found in Zebker et al. (1994), Bamler and Hartl (1998), Henderson and Lewis (1998), Massonnet and Feigl (1998), Rosen et al. (2000), Hensley et al. (2001), and Hanssen (2001). Interested readers should consult these references.

19.2.4 InSAR Image Interpretation and Modeling

To understand geophysical processes that cause the observed surface deformation, numerical models are often employed to infer physical parameters of deformation sources based on the observed deformation. The spatial resolution of surface displacement data provided by InSAR makes it possible to constrain different deformation models. For earthquake studies, the dislocation source (Okada, 1985) is commonly used. For volcano studies, a variety of source geometries, such as the spherical point pressure source (Mogi source) (Mogi, 1958), the dislocation source (sill or dike source) (Okada, 1985), the ellipsoid source (Davis, 1986; Yang et al., 1988), the penny-crack source (Fialko et al., 2001), etc. can be used to model ground-surface deformation due to magmatic activity. The most widely used source in volcano deformation modeling is the spherical point pressure source (also called Mogi source) embedded in an elastic homogeneous half-space (Mogi, 1958). The predicted displacement (u) at the free surface of an elastic homogeneous half-space due to a change in volume (ΔV) or pressure (ΔP) of a sphere (i.e., a presumed magma reservoir) is

$$u_i(x_1 - x_1', x_2 - x_2', -x_3) = C\frac{x_i - x_i'}{\left|R^3\right|} \tag{19.12}$$

where x_1', x_2', and x_3' are the horizontal locations and depth of the center of the sphere, R is the distance between the sphere and the location of observation (x_1, x_2, and 0), and C is a combination of material properties and source strength

$$C = \Delta P(1 - v)\frac{r_s^3}{G} = \Delta V\frac{(1 - v)}{\pi} \tag{19.13}$$

where ΔP and ΔV are the pressure and volume changes of the magma chamber, respectively, v is Poisson's ratio of the host rock (typical value of 0.25), r_s is the radius of the reservoir sphere, and G is the shear modulus (Delaney and McTigue, 1994; Johnson, 1987).

A nonlinear least-squares inversion approach is often used to optimize the source parameters in Equations 19.12 and 19.13 (Cervelli et al., 2001; Press et al., 1992). Modeling the observed interferogram in Figure 19.1h using a Mogi source results in a best-fit source located at a depth of 6.5 ± 0.2 km. The calculated volume change is 0.043 ± 0.002 km^3. Figure 19.1i shows the

modeled interferogram based on the best-fit source parameters. It is obvious that the Mogi source fits the observed deformation in Figure 19.1h very well.

19.2.5 InSAR Products

Typical InSAR processing includes precise registration of an interferometric SAR image pair, interferogram generation, removal of curved Earth phase trend, adaptive filtering, phase unwrapping, precise estimation of interferometric baseline, generation of a surface deformation image (or DEM map), estimation of interferometric correlation, and rectification of interferometric products. Using a single pair of SAR images as input, a typical InSAR processing chain outputs two SAR intensity images, a deformation or DEM map, and an interferometric correlation image.

19.2.5.1 SAR Intensity Image

SAR intensity images are sensitive to terrain slope, surface roughness, and target dielectric constant. Surface roughness refers to the SAR wavelength-scale variation in the surface relief, and the radar dielectric constant is an electric property of material that influences radar return strength. Therefore, SAR intensity images alone can be used to map hazards-related landscape changes, whether natural or manmade. Multiple-temporal SAR intensity images can be used to monitor the progression of landscape changes due to hazards such as flooding, wildfire, volcanic eruption, earthquake shaking, or landslide. In cloud-prone areas, all-weather SAR intensity imagery can be the most useful data source available to track the course of hazardous events.

19.2.5.2 InSAR Coherence Image

An InSAR coherence image is a cross-correlation product derived from two coregistered complex-valued (both intensity and phase components) SAR images (Lu and Freymueller, 1998; Zebker and Villasenor, 1992). It depicts changes in backscattering characteristics on the scale of radar wavelength. Loss of InSAR coherence is often referred to as decorrelation. Decorrelation can be caused by the effects of (1) thermal decorrelation caused by uncorrelated noise sources in radar instruments, (2) geometric decorrelation resulting from imaging a target from different look angles, (3) volume decorrelation caused by volume backscattering effects, and (4) temporal decorrelation due to environmental changes over time (Lu and Kwoun, 2008; Zebker and Villasenor, 1992). Decorrelation renders an InSAR image useless for measuring ground-surface deformation. On the one hand, geometric and temporal decorrelation can be mitigated by choosing an image pair with short baseline and brief temporal separation, respectively, so choosing such a pair is recommended when the goal is to measure surface deformation, for example. On the other, the pattern of decorrelation within an image can indicate

surface modifications caused by flooding, wildfire, volcanic eruption, or earthquake shaking. In this way, time-sequential InSAR coherence maps can be used to map the extent and progression of hazardous events.

19.2.5.3 InSAR Deformation Image

Unlike a SAR intensity image, an InSAR deformation image is derived from phase components of two overlapping SAR images. SAR is a side-looking sensor, so an InSAR deformation image depicts ground-surface displacements in the SAR line-of-sight (LOS) direction, which include both vertical and horizontal motion. Typical look angles for satellite-borne SARs are less than 45° from vertical, so LOS displacements in InSAR deformation images are more sensitive to vertical motion (uplift/subsidence) than horizontal motion. Here and henceforth we conform to common usage by sometimes using the terms "displacement" and "deformation" interchangeably. Readers should keep in mind that, strictly speaking, displacement refers to a change in position (e.g., LOS displacement of a given resolution element or group of elements in an InSAR image), whereas deformation refers to differential motion among several elements or groups (i.e., strain). The spatial distribution of surface deformation data from InSAR images can be used to constrain numerical models of subsurface deformation sources. By comparing the deformation patterns predicted by such idealized sources to the actual patterns observed with InSAR, one can identify a best-fitting source. InSAR deformation images have an advantage for modeling purposes over point measurements made with GPS, for example, because InSAR images provide more complete spatial coverage than is possible with even a dense network of GPS stations. On the other hand, continuous GPS stations provide better precision and much better temporal resolution than is possible with InSAR images, which is constrained by the orbital repeat times of SAR satellites. For hazards monitoring, a combination of periodic InSAR observations and continuous data streams from networks of *in situ* instruments is ideal.

19.2.5.4 Digital Elevation Model

As described earlier, the ideal SAR configuration for DEM production is a single-pass (simultaneous) two-antenna system (e.g., SRTM). However, repeat-pass single-antenna InSAR also can be used to produce useful DEMs. Either technique is advantageous in areas where the photogrammetric approach to DEM generation is hindered by persistent clouds or other factors (Lu et al., 2003a). There are many sources of error in DEM construction from repeat-pass SAR images, for example, inaccurate determination of the InSAR baseline, atmospheric delay anomalies, possible surface deformation due to tectonic, volcanic, or other sources during the time interval spanned by the images, etc. To generate a high-quality DEM, these errors must be identified and corrected using a multi-interferogram approach (Lu et al., 2003a). A data fusion technique

such as the wavelet method can be used to combine DEMs from several interferograms with different spatial resolution, coherence, and vertical accuracy to generate the final DEM product (Baek et al., 2005; Ferretti et al., 1999).

19.3 Issues in InSAR Processing

19.3.1 Phase Anomalies due to SAR Processor

A SAR processor is required to transform a scene of raw SAR data into an SLC image through the matched filtering of raw SAR data in both range and azimuth directions with corresponding reference functions (e.g., Curlander and McDonough, 1991). However, imperfect geometric calculations could result in a ramping phase in an InSAR image. Figure 19.3 shows two InSAR images processed with two different SAR processors. The ramping phase in Figure 19.3a is likely due to SAR processing error. Note that this ramping phase can be easily confused with that caused by baseline error (see Section 19.2.3).

19.3.2 InSAR Coherence Improvement

Interferometric coherence is a qualitative assessment of the correlation of SAR images acquired at different times. It determines the amount of phase error and thus the accuracy of deformation estimates or DEM products. Constructing a coherent interferogram requires that SAR images must correlate with each other; that is, the backscattering spectrum must be substantially similar over the observation period. Physically, this translates into a requirement that the ground scattering surface be relatively undisturbed at the radar wavelength scale between measurements (Li and Goldstein, 1990; Zebker and Villasenor, 1992). The comparison of L-band and C-band interferometric coherence suggests that L-band is far superior to C-band for surfaces covered with thick vegetation or loose material (Lu, 2007; Lu et al., 2005a, 2005b). Therefore, chances for producing coherent interferograms are assured by using C-band images separated in time by a few months to a few years over sparsely vegetated terrains and by using L-band imagery over surfaces with thick vegetation or loose material (Figure 19.4).

Another factor that can enhance InSAR coherence is image coregistration. One stringent prerequisite in InSAR processing is the precise registration of reference and slave SAR images and resampling the slave image to the geometry of the reference image. For conventional InSAR processing, coregistration is done by cross-correlating the reference and slave images at a dense grid of pixel locations and using the results to construct range and azimuth offset polynomials for the entire image. The range and azimuth offset polynomials are expressed as functions of range and azimuth pixel position. A problem arises when, for an interferogram with a large perpendicular

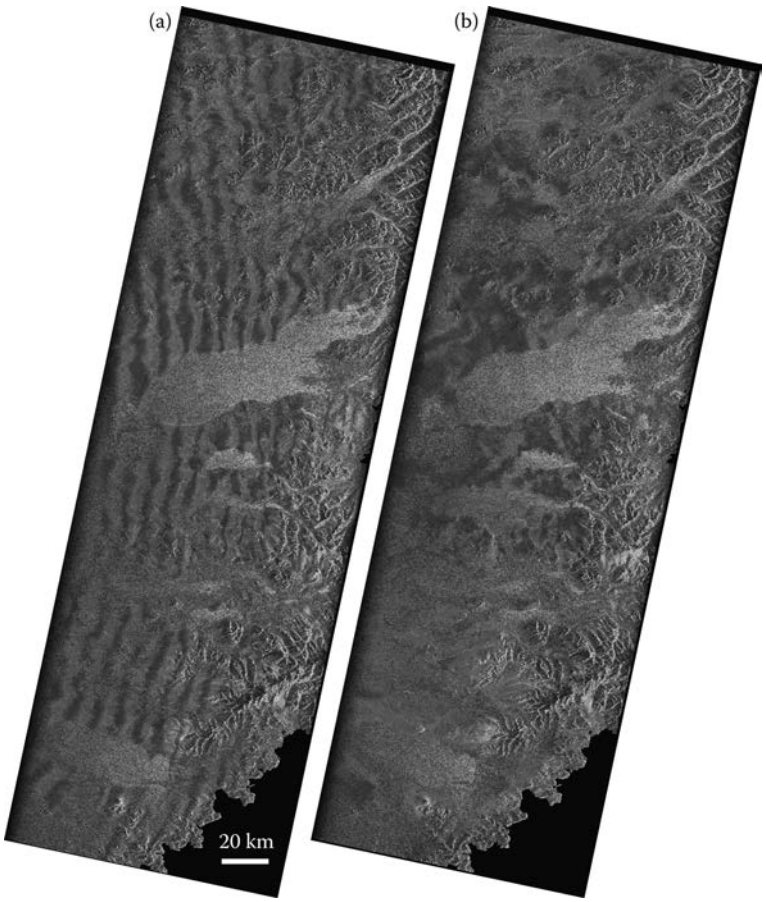

FIGURE 19.3
Interferograms produced from two different SAR processors based on the same pair of SAR images. The ramping fringes in Figure 19.2a are likely due to the systematic phase error in SAR processing.

baseline, topographic variations introduce additional localized offsets between the reference and slave images (Lu and Dzurisin, 2010). The range offset due to topographic relief is linearly dependent on topography and can be approximated as

$$\Delta r_{\text{off}} = -\frac{B_{\perp}}{H \tan \theta} \Delta h \tag{19.14}$$

where Δr_{off} is the range offset due to height difference Δh, $B_{\perp}$ is the perpendicular baseline of the interferogram, H is the altitude of the satellite above Earth, and θ is the SAR look angle. For the ERS and Envisat SAR sensor, normal values for H and θ are about 790 km and 23° (beam mode IS2 for

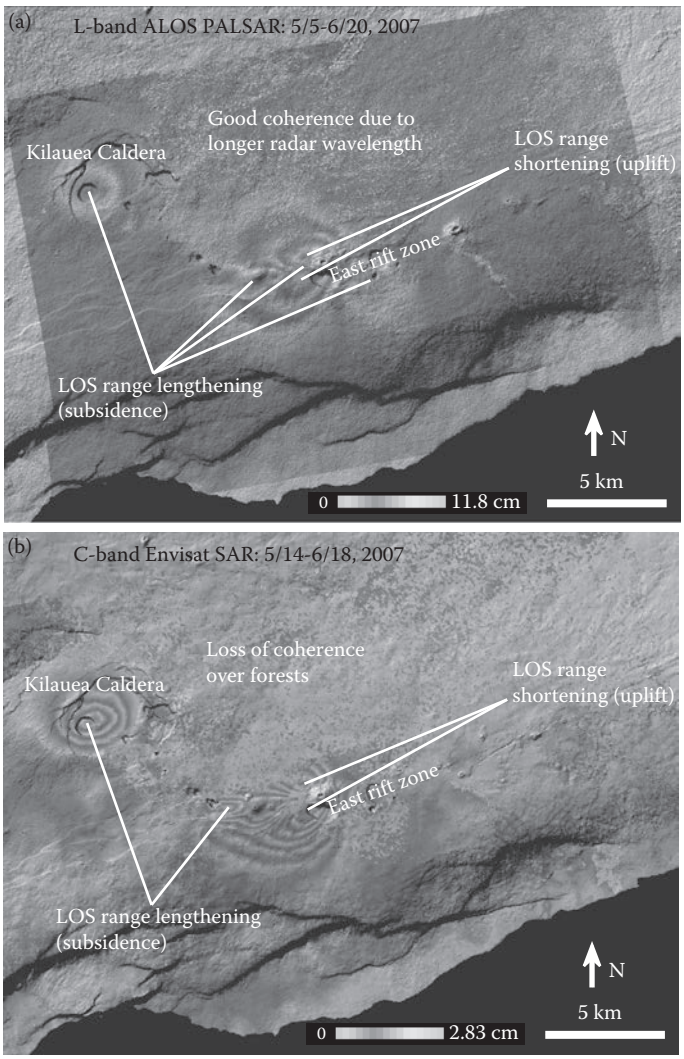

FIGURE 19.4
(**See color insert.**) (a) L-band ALOS and (b) C-band Envisat InSAR images capturing ground-surface deformation associated with the June 2007 eruption at Kilauea volcano. Each fringe (full color cycle) represents a line-of-sight range change of 11.8 and 2.83 cm for ALOS and Envisat interferograms, respectively. InSAR deformation values are draped over the shaded relief map. Areas of loss of coherence are not colored. Note that C-band InSAR image loses coherence over areas of dense vegetation.

Envisat), respectively. A 1 km difference in topography can induce about ~1.5 m range offset for an Envisat interferogram with a perpendicular baseline of 500 m. This offset is about 8% of the range pixel size. For the ALOS PALSAR sensor, normal values for H and θ are about 700 km and 34°, respectively. The

topography-induced range offset for a fine-beam PALSAR interferogram with a perpendicular baseline of 1 km can be as large as ~2.1 m, or about 23% of the range pixel size. In other words, range offsets due to topographic relief over rugged terrains can be large enough to degrade InSAR coherence if the offsets are not taken into account during image coregistration. Therefore, we recommend using a DEM and the SAR imaging geometry to compute direct functions that map the position of each pixel in the reference image to a corresponding pixel location in the slave image. This can result in significant improvement in coherence for interferograms with relatively large baselines (Lu and Dzurisin, 2010).

19.3.3 InSAR Baseline

A significant error source in InSAR deformation mapping is baseline uncertainty due to inaccurate determination of SAR antenna positions. For ERS-1, ERS-2, Envisat, ALOS, and TerraSAR-X satellites, the refined precision orbit data should be used for InSAR processing. The accuracy of the satellite position vectors provided in RADARSAT-1 and JERS-1 metadata is much poorer than that for ERS-1, ERS-2, Envisat, ALOS, and TerraSAR-X. Therefore, baseline refinement is particularly required for RADARSAT-1 or JERS-1 interferogram processing. Even for ERS-1, ERS-2, and Envisat satellites where precise restitute vectors are available, baseline errors in interferograms can often be present. Figure 19.2a is an interferogram of Okmok Volcano from a pair of ERS-2 images acquired on August 18, 2000, and July 19, 2002. The precision position vectors are used for the InSAR processing. The apparent range changes due to baseline errors are obvious, and the volcanic deformation over the island can be easily confused as there are more than three fringes outside the 10-km-wide caldera. Therefore, interferogram baselines should be refined for InSAR deformation mapping. A commonly used method is to determine the baseline vector based on an existing DEM via a least-squares approach (Rosen et al., 1996). In this approach, areas of the interferogram that are used to refine the baseline should have negligible deformation or known deformation from an independent source. Assuming the deformation away from the caldera is insignificant in the interferogram in Figure 19.5a, the baseline for this interferogram can be refined. Figure 19.5b shows the deformation interferogram produced with the refined baseline for the interferogram shown in Figure 19.5a. Volcanic deformation of more than three fringes (about 8–10 cm inflation) over the island can be observed from this interferogram, and it now becomes obvious that most of the deformation occurred within the caldera (Figure 19.5b).

19.3.4 Atmospheric Artifacts

A significant error source in repeat-pass InSAR deformation measurement is due to atmospheric delay anomalies caused by small variations in the index

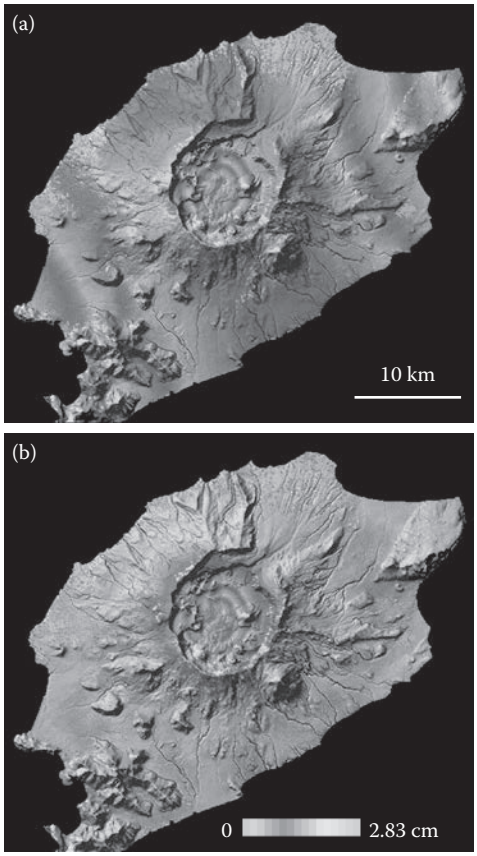

FIGURE 19.5
Topography-removed interferograms of Okmok Volcano, Alaska (a) before and (b) after baseline refinement. Each interferometric fringe (full-color cycle) represents a 2.83-cm range change between the ground and the satellite.

of refraction along the line of propagation. Spaceborne SAR sensors such as ERS-1/-2, JERS-1, RADARSAT-1, Envisat, ALOS, and TerraSAR-X satellites orbit at altitudes of about 600–800 km. The electromagnetic wave from these sensors must propagate through the ionosphere, the stratosphere, and the troposphere. Therefore, the radar pulses are subject to small variations in the index of refraction along the line of propagation. Changes in temperature, pressure, and water vapor content of the atmosphere during the two observation instances will result in variations of phase of signals. These variations introduce errors in the observed interferogram. Zebker et al. (1997) indicated that variations of atmospheric water vapor contributed the most to atmospheric anomaly delays. Spatial and temporal changes of 20% in relative humidity could lead to 10-cm errors in repeat-pass interferometric deformation maps.

Over cloud-prone and rainy regions, the range change caused by atmospheric delays can be significant. Figure 19.6a shows a topography-removed interferogram, covering the southeastern part of Okmok Volcano, Alaska. This topography-removed interferogram is constructed using a pair of SAR images acquired in May and July 1997, respectively. Range change up to about 5 cm is observable. To confirm that the range changes in Figure 19.6a were caused by a difference in atmospheric conditions rather than by volcanic activity, another two interferograms were generated for the same area: one interferogram (Figure 19.6b) was produced using the image acquired in July 1997 (which was used in Figure 19.6a) and an image acquired in September 1997; the other interferogram (Figure 19.6c) was produced using the May and September 1997 images. In Figure 19.6b, apparent fringes similar to that in the May–July interferogram (Figure 19.6a) were observed. Because the change in color in Figure 19.6a is opposite that in Figure 19.6b, and because no fringe was observed in the May–September interferogram (Figure 19.6c), it is concluded that the fringes in Figure 19.6a and b were most

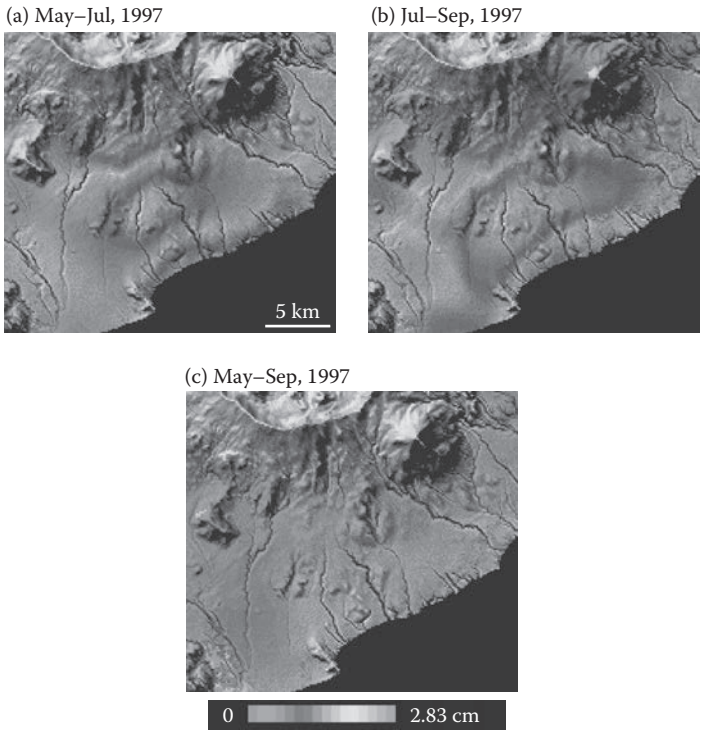

FIGURE 19.6
A portion of a topography-removed interferogram of Okmok Volcano, Alaska shows severe atmospheric anomalies associated with the July 1997 acquisition used for interferograms in (a) and (b).

likely caused by an atmospheric anomaly that occurred primarily on the July 1997 image. Therefore, multiple observations from independent interferograms for similar time intervals should be used to verify any apparent deformation (Lu et al., 2000; Zebker et al., 1997). Because atmospheric artifacts do not correlate in time, multi-interferogram InSAR processing (see Section 19.4) can be used to model and reduce atmospheric noise and enhance the signal-to-noise ratio of the deformation signal.

There are three kinds of techniques proposed to estimate the water vapor content from external sources/images and remedy the atmospheric effect on deformation interferograms. The first method is to estimate water vapor concentrations in the target area at the times of SAR image acquisitions using short-term predictions from operational weather models (e.g., Foster et al., 2006). Predicted atmospheric delays from the weather model are used to generate a synthetic interferogram that is subtracted from the observed interferogram, thus reducing atmospheric delay artifacts and improving the ability to identify any remaining ground deformation signal. The problem with this approach is that the current weather models have much coarser resolution (a few kilometers) than InSAR measurements (tens of meters). This deficiency can be remedied to some extent by integrating weather models with high-resolution atmospheric measurements, but this approach requires intensive computation. The second method is to estimate water vapor concentration from continuous Global Positioning System (CGPS) observations in the target area. CGPS is capable of retrieving precipitable water vapor content along the satellite-to-ground LOS with an accuracy that corresponds to 1–2 mm of surface displacement (Bevis et al., 1992; Niell et al., 2001). The spatial resolution (i.e., station spacing) of local or regional CGPS networks is typically several kilometers to a few tens of kilometers, which is sparse relative to the decimeter-scale spatial resolution of SAR images. Therefore, spatial interpolations that take into account the covariance properties of CGPS zenith wet delay (ZWD) measurements and the effect of local topography are required. Jarlemark and Emardson (1998) applied a topography-independent, turbulence-based method to spatially interpolate ZWD values. In a follow-up study, Emardson et al. (2003) found that the spatio-temporal average variance of water vapor content depends not only on the distance between GPS observations, but also on the height difference between stations (i.e., topography). These and other studies led to a topography-dependent turbulence model for InSAR atmospheric correction using ZWD values from CGPS data (Li et al., 2005). The third approach to correcting atmospheric delay anomalies in InSAR observations is to utilize water vapor measurements from optical satellite sensors such as the Moderate Resolution Imaging Spectroradiometer (MODIS), Advanced Spaceborne Thermal Emission and Reflection Radiometer (ASTER), and European Medium Resolution Imaging Spectrometer (MERIS) (Li et al., 2003). The disadvantage of this method is the requirement of nearly simultaneous acquisitions of SAR and cloud-free optical images.

19.3.5 Ionospheric Artifacts

It has been demonstrated that fluctuations in ionospheric electron density can result in modulations in SAR and InSAR images (Gray et al., 2000; Mattar and Gray 2002; Meyer et al., 2006; Wegmuller et al., 2006). The ionospheric disturbance on InSAR images could produce azimuth pixel shift in SAR image correlation and can affect a region of a few kilometers in scale. Accordingly, interferometric phase values over the affected region are also biased. The ionospheric effect is more pronounced over regions of strong magnetic disturbance. The effects are more severe on long-wavelength SAR (e.g., L-band) than short-length SAR (e.g., C-band). Figure 19.7b shows the image offset in azimuth direction by correlating the two SAR images used to produce the interferogram (Figure 19.7a) over northern Alaska. Azimuth offsets range from –5 to 10 m. This is mostly likely caused by ionosphere

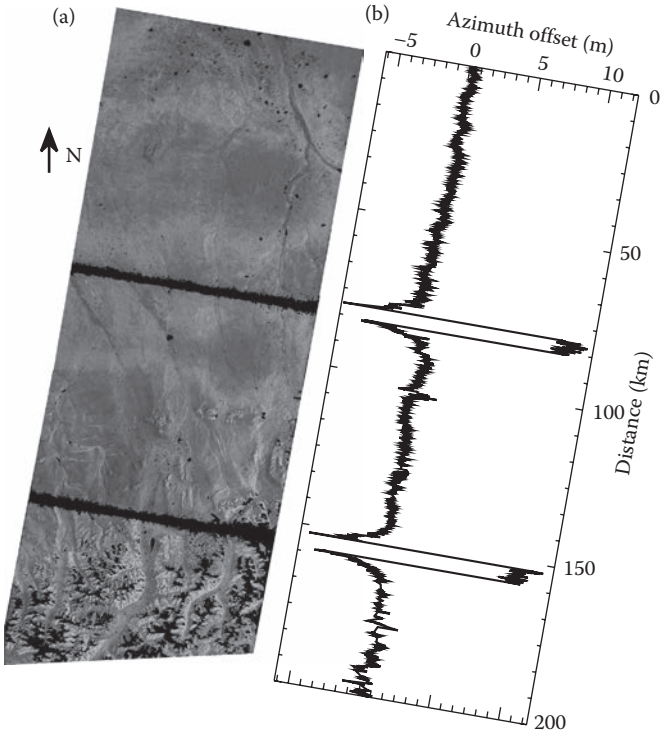

FIGURE 19.7
(a) An interferogram of northern Alaska from a pair of L-band JERS-1 SAR images of June 17 and July 31, 1996. The horizontal stripes of uncolored areas represent loss of InSAR coherence due to extreme azimuth offsets caused by ionospheric anomalies. (b) Azimuth offsets between two JERS-1 images used to generate the interferogram in (a). The azimuth offsets, which are most likely due to ionospheric disturbance, render loss of interferogram coherence over ionosphere-affected areas.

disturbance at the times when the SAR images were acquired. The ionospheric anomalies affect not only the azimuth offset but also the interferogram phase by introducing phase delays as well as reducing the coherence of interferogram (Figure 19.7a). Even though the interferogram coherence can be improved by taking into account the localized offset anomalies (Wegmuller et al., 2006), the phase anomalies cannot be easily removed. Research on removing ionosphere effects in InSAR phase variations is an ongoing hot topic (Meyer et al., 2010).

19.4 Multi-Interferogram InSAR Processing

Multi-interferogram InSAR (Berardino et al., 2002; Ferretti et al., 1999, 2001; Hooper et al., 2007; Rocca 2007) is one of the most significant recent advances in InSAR image fusion to improve deformation measurement accuracy for improved hazards assessment and monitoring. "Multi-" in this context refers to a series of InSAR observations in time, thus affording the opportunity to recognize spurious effects. The objective is to fuse multiple-interferogram measurements of the same area to characterize the spatial and temporal behaviors of the deformation signal and various artifacts and noise sources (atmospheric delay anomalies, orbit errors, DEM-induced artifacts), then to remove the artifacts and anomalies to retrieve time-series deformation measurements at the SAR pixel level.

Among several approaches to multi-interferogram analysis, persistent scatterer InSAR (PSInSAR) is one of the newest and most promising data fusion techniques. PSInSAR uses the distinctive backscattering characteristics of certain ground targets (PS) and unique characteristics of atmospheric delay anomalies to improve the accuracy of conventional InSAR deformation measurements (Ferretti et al., 1999, 2001). The SAR backscattering signal of a PS target has a broadband spectrum in the frequency domain, implying that the radar phase of this kind of scatterer correlates over much longer time intervals and over much longer baselines than other scatterers. As a result, if the backscatter signal from a given pixel is dominated by return from one or more PS(s), the pixel remains coherent over long time intervals. Therefore, at PS pixels, the limitation imposed by loss of coherence in conventional InSAR analysis can be overcome. Because InSAR coherence is maintained at PS pixels, the atmospheric contribution to the backscattered signal, DEM error, and orbit error can be identified and removed from the data using a multi-interferogram iterative approach. After these errors are removed, displacement histories at PS pixels can be resolved with millimeter accuracy (Figure 19.8) (Lee et al., 2010). If a sufficient number of PS pixels exist in a series of interferograms, relative displacements among them can provide a relatively detailed picture of the surface deformation field.

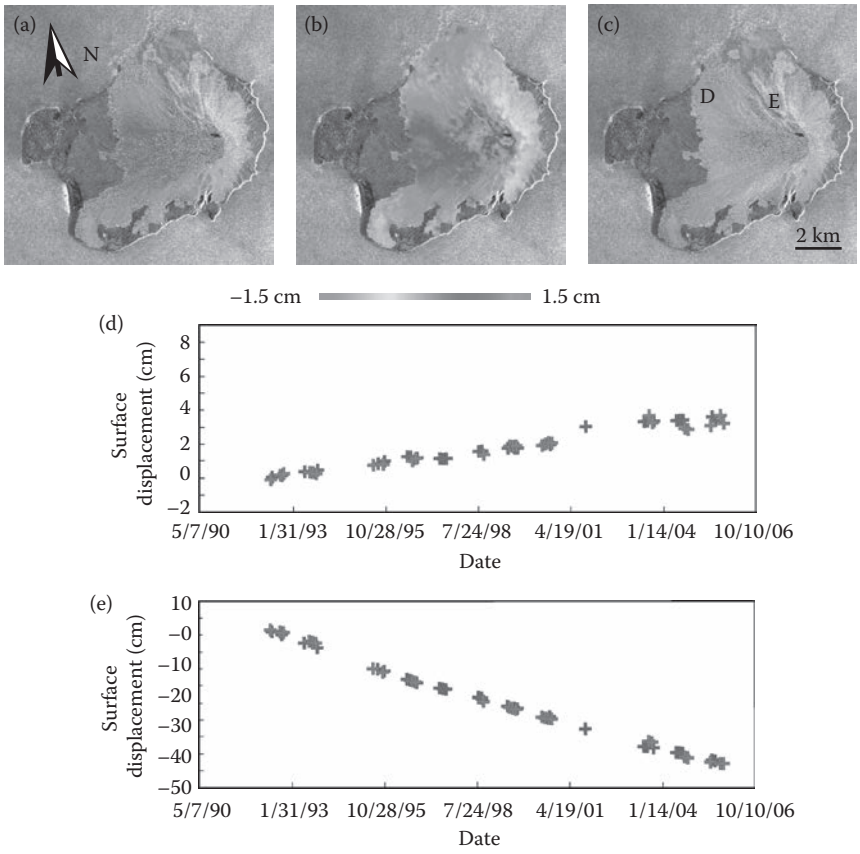

FIGURE 19.8
An example of multi-interferogram InSAR processing to improve deformation mapping. (a) An observed interferogram of Augustine Volcano, Alaska, from two SAR images acquired on June 5, 1992, and July 30, 1993. (b) A synthetic interferogram showing range changes due to atmospheric effects. This image is produced using spatial low-pass and temporal high-pass filtering during multi-interferogram InSAR processing. (c) Refined InSAR image after multi-interferogram processing, which effectively removes artifacts due to baseline and atmospheric delay anomalies in (a). (d, e) Line-of-sight (LOS) time-series surface displacements at points D and E (c) during 1992–2005. Red and purple symbols indicate time-series displacement histories that are produced by multi-interferogram InSAR processing of ERS-2 SAR images from tracks 229 and 501, respectively. Ground surface at location D inflated at a rate of 3 mm/year presumably due to magma intrusion while ground surface at E subsided at a rate of 3 cm/year due to thermal compaction of the pyroclastic flows from 1986 eruption. (Adapted from Lee, C.W., Z. Lu, H.S. Jung, J.S. Won, and D. Dzurisin. 2010. Surface deformation of Augustine Volcano (Alaska), 1992–2005, from multiple-interferogram processing using a refined SBAS InSAR approach. USGS Professional Paper, in press.)

19.5 Application of InSAR Imagery to Monitor Natural Hazards in Protected Lands

19.5.1 DEM Generation

A precise digital elevation model can be a very important dataset for characterizing, monitoring, and mitigating various natural hazards in protected lands. For example, a DEM is needed to simulate potential mudflows (lahars) that are commonly associated with volcanic eruptions, large earthquakes, and flooding caused by heavy rainfall. As described earlier, the ideal SAR configuration for DEM production is a single-pass (simultaneous) two-antenna system (Farr et al., 2007). However, repeat-pass single-antenna InSAR also can be used to produce useful DEMs (Ruffino et al., 1998, Sansosti et al., 1999). Either technique is advantageous in areas where the photogrammetric approach to DEM generation is hindered by persistent clouds or other factors (Lu et al., 2003a). To generate a high-quality DEM, a multi-interferogram approach is needed to identify and correct various artifacts in repeat-pass InSAR imagery (Lu et al., 2003a). One example of the utility of precise InSAR-derived DEMs is illustrated in Figure 19.9, which shows the extent and thickness of a lava flow extruded during the 1997 Okmok eruption. The flow's three-dimensional (3-D) distribution was derived by differencing two DEMs that represent the surface topography before and after the eruption. Multiple repeat-pass interferograms were used to correct various error sources and generate the high-quality DEMs (Lu et al., 2003a).

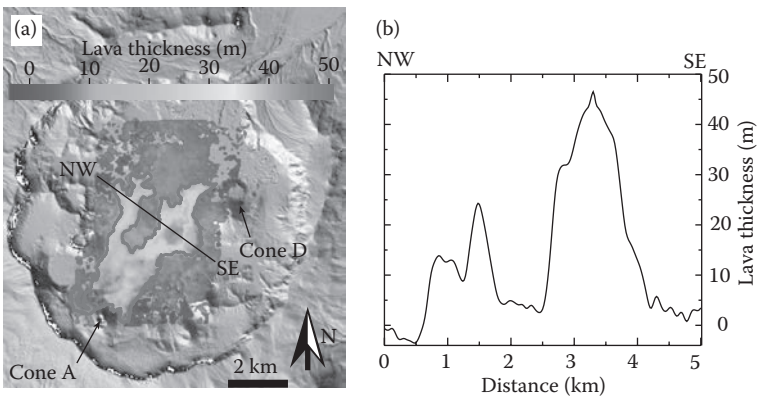

FIGURE 19.9
Thickness of lava flows emplaced during the April 1997 eruption at Okmok Volcano, Alaska. Flow thickness was derived from the height difference between preeruption and posteruption DEMs that were constructed from multiple interferograms. (b) Lava thickness along profile S–S′, which reached nearly 50 m in the thickest part of the flow (orange tones near center of image). Q4

19.5.2 Mapping Volcanic Deformation

Volcanic deformation patterns can provide an important insight into the structure, plumbing, and state of restless volcanoes, and can be the first sign of increasing unrest that might include earthquake swarms or other precursors to an impending intrusion or eruption (Dzurisin, 2007). Here we show an example of how multitemporal InSAR images can be used to monitor volcanic activity and construct a magma plumbing system.

Okmok Volcano, a broad shield volcano in protected lands over the central Aleutian, produced blocky, basaltic flows during relatively large, effusive eruptions in 1945, 1958, and 1997 from Cone A, and a hydrovolcanic eruption in 2008 from near Cone D (Figure 19.10) (Lu et al., 1998, 2000, 2005a, 2010). InSAR images constructed from ERS-1, ERS-2, RADARSAT-1 and Envisat SAR data depict volcanic deformation before, during, and after the 1997 eruption and prior to the 2008 eruption (Figure 19.10). More than five fringes appear inside the caldera in the 1992–1993 interferogram (Figure 19.10a), but only two fringes appear in the 1993–1995 interferogram (Figure 19.10b). It can be inferred from these two interferograms that the center of the caldera rose more than 14 cm during 1992–1993 and about 6 cm during 1993–1995. The 1995–1996 interferogram (Figure 19.10c) indicates that the caldera subsided 1 ~ 2 cm between 1.5 and 0.5 years before the 1997 eruption. Therefore, the preeruption inflation rate decreased with time during 1992–1995, and inflation stopped sometime during 1995–1996. More than 140 cm of surface deflation associated with the 1997 eruption can be inferred from the ERS interferogram (Figure 19.10d). The deflation presumably is due to the withdrawal of magma during the 1997 eruption (Lu et al., 1998, 2000, 2005a, 2010). Progressive posteruptive inflation rates generally decreased with time during 1997–2001 (Figure 19.10e through h): from ~10 cm/year during 1997–1998 to ~8 cm/year during 1998–2000 and ~4 cm/year during 2000–2001. Then the
Q3 inflation rate increased to ~12 cm/year during 2001–2002 (Figure 19.10i)and reached a maximum of ~17–20 cm/year during 2002–2004 (Figure 19.10j and k). The inflation trend was interrupted during 2004–2005, when ~3–5 cm of subsidence occurred (Figure 19.10l). A similar amount of uplift occurred during 2005–2006 (Figure 19.10m), followed by nearly no volcano-wide deformation during 2006–2007 (Figure 19.10n). About 15 cm of uplift occurred from summer 2007 to July 10, 2008, shortly before the July 12, 2008 eruption (Figure 19.10o). Based on the shape and radial pattern of the displacement field, Lu et al. (2005a, 2010) assumed that deformation was caused by a volume change in a spherical magma reservoir, and modeled the surface displacement field using a point source within a homogenous isotropic elastic half-space (Mogi, 1958). Point-source models indicate that a magma reservoir at a depth of 3.2 km below sea level, located beneath the center of the caldera, is responsible for the observed volcano-wide deformation. Magma filled this reservoir at a rate that varied both before and after the eruption, causing volcano-wide inflation. When the magma pressure within the reservoir reached a certain

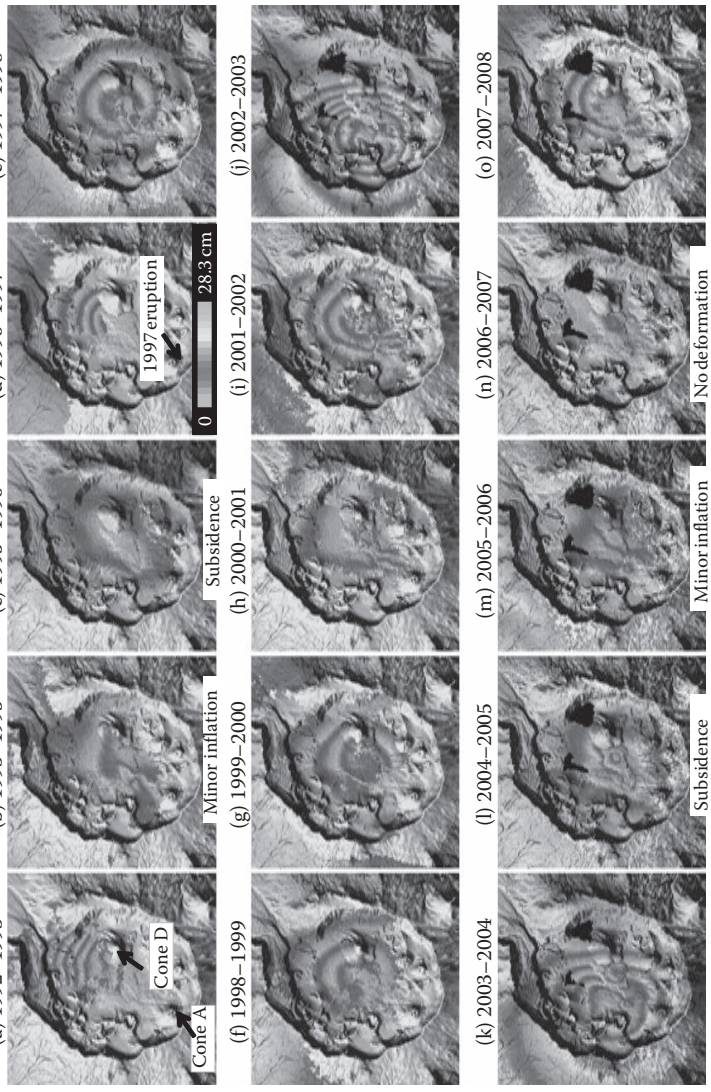

FIGURE 19.10
(See color insert.) Deformation interferograms of Okmok Volcano for the periods (a–c) before, (d) during, and (e–o) after the 1997 eruption. Areas of loss of radar coherence are uncolored. Unless otherwise noted, each interferometric fringe (full-color cycle) represents a 2.83-cm range change between the ground and the satellite.

threshold, an eruption ensued. Withdrawal of magma via an eruption depressurized the reservoir, causing volcano-wide deflation, and fed surface lava flows. Magma started to accumulate in the reservoir soon after the eruption stopped, initiating a new intereruption strain cycle.

19.5.3 Mapping Earthquake Displacement

Frequent earthquakes shake the protected lands. Using a pair of SAR images, one acquired before the earthquake and the other after the earthquake, InSAR can be used to map the co-seismic deformation field, and in turn to estimate earthquake location, fault geometry, and rupture dynamics (Figure 19.11). Multiple-temporal InSAR images can be used to estimate interseismic strain accumulation, which is crucial to understanding continental deformation, the earthquake cycle, and seismic hazards (Biggs et al., 2007). InSAR can map ground-surface deformation immediately after an earthquake (i.e., postseismic deformation), which yields important information for inferring properties of the Earth's crust and upper mantle (e.g., Biggs et al., 2009). InSAR is playing an increasingly important role in mapping triggered slip, which occurs during an earthquake on faults not involved in the main shock and therefore is extremely difficult to capture with conventional geodetic techniques (e.g., Fialko et al., 2002). In addition, InSAR can identify blind faults (i.e., buried faults that do not intersect the ground surface) from

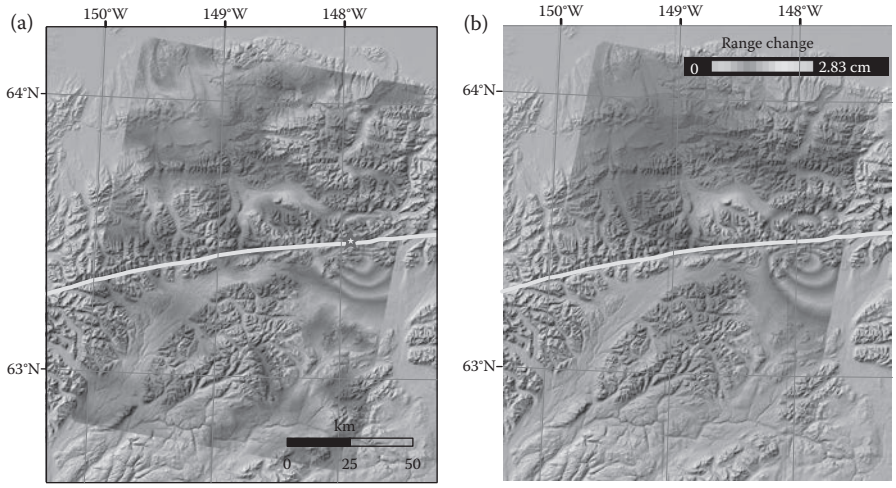

FIGURE 19.11
(a) RADARSAT-1 InSAR image (August 16–October 27, 2002) showing coseismic ground-surface deformation associated with the October 23, 2002, *M* 6.7 Nenana Mountain earthquake along the Denali Fault (yellow line), Alaska (). (Adapted from Lu, Z., T. Wright, and C. Wicks. 2003b. Deformation of the 2002 Denali Fault earthquakes, Alaska, mapped by RADARSAT-1 interferometry. *EOS Trans*., 84:425–431.) (b) Modeled InSAR image using fault parameters that best fit the observed interferogram shown in (a).

Q11, Q12

surface deformation patterns. Furthermore, loss of InSAR coherence images can be used to infer ground damages (e.g., Fielding et al., 2005). Combined with seismology and other geophysical and geodetic techniques, InSAR can be expected to foster many breakthroughs in understanding the physics of the earthquake cycle (Wright, 2002).

19.5.4 Landslide Monitoring

Landslides in protected lands constitute a major natural hazard. InSAR can be used to map movement of landslides (Figure 19.12). InSAR's remote sensing capability provides a nonintrusive way to monitor landslide hazards in protected lands. Ground-surface deformation associated with landslide movement, when combined with other observation and analysis, can render a better understanding of landslide behavior and contribute more effective procedures to reduce landslide hazards.

19.5.5 Glacier Monitoring

Monitoring changes in glaciers and ice sheets can provide an improved understanding on their role in global warming and sea level rise. InSAR has been used to record the movement of glaciers and ice fields, and has significantly advanced the study of glacier, ice flow, and ice-sheet mass balance (Figure 19.13). InSAR can not only determine ice velocity and discharge by ice streams and glaciers and quantify their contributions to sea-level rise, but

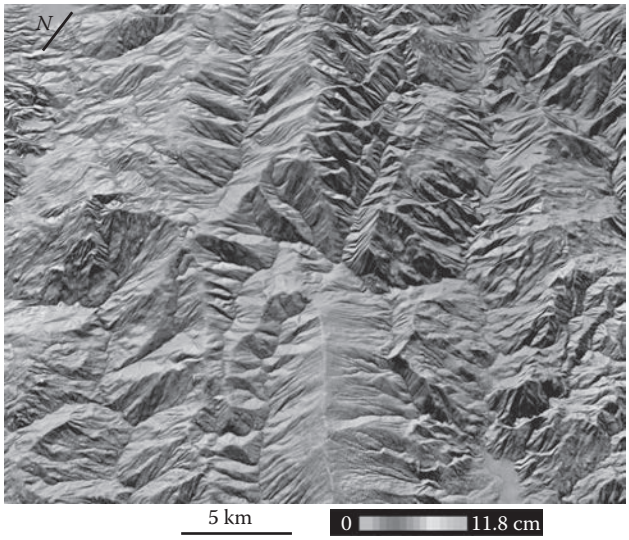

FIGURE 19.12
An L-band PALSAR InSAR image showing landslide movement over Six Rivers National Forest in northern California during April 29 and July 30, 2007.

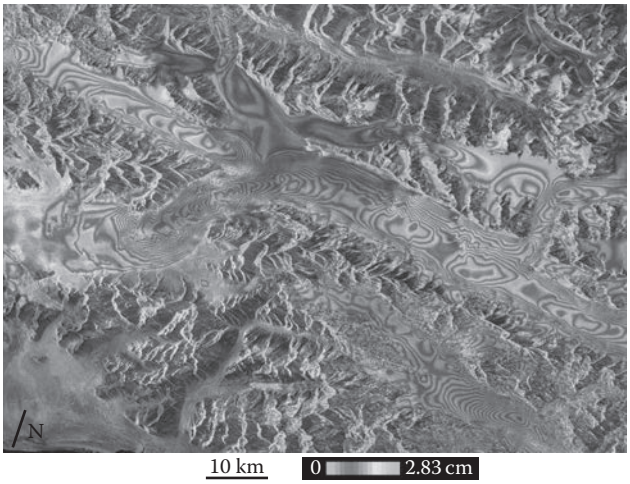

FIGURE 19.13
Interferogram showing movement of Wrangell glaciers over southern Alaska in 24 h between March 31 and April 1, 1996. The interferometric phase image is draped over the radar intensity image. Each fringe (full-color cycle) represents a 2.8-cm change in range distance.

also characterize the temporal variability in ice flow well enough to separate short-term fluctuations from long-term change (Rignot and Thomas, 2002).

19.5.6 Fire Scar Mapping

Fires occur frequently on protected lands. InSAR images and their associated products (e.g., SAR intensity images and InSAR coherence images) have proven useful for mapping landscape changes (Kwoun and Lu, 2009; Ramsey et al., 2006). Wildfires modify vegetation structure as well as moisture conditions that induce changes in SAR backscattering signal. Therefore, multiple SAR images can be used to map the progression of fire and to estimate fire severity (Figure 19.14). InSAR products that characterize changes in SAR backscattering return (both intensity and coherence images) are indispensable for precise mapping of fire scar extents and severities (Rykhus and Lu, 2010). Similarly, SAR and InSAR coherence images provide all-weather imaging capability for flood monitoring over protected lands (Rykhus and Lu, 2007).

19.6 Conclusions

The satellite InSAR technique has proven to be a powerful all-weather remote sensing tool for monitoring and studying a variety of geological hazards in protected lands by analyzing surface deformation patterns

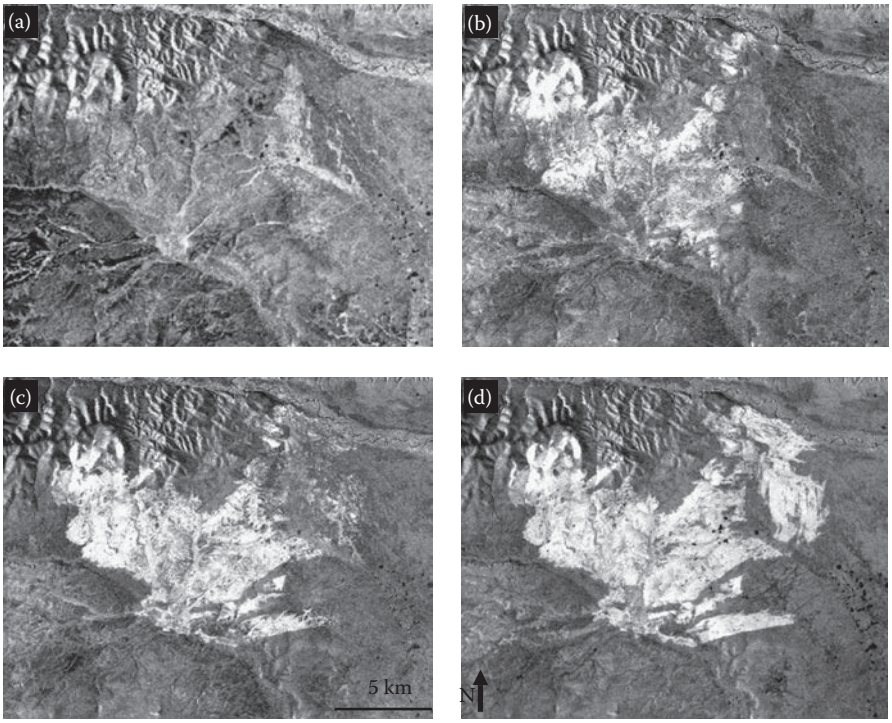

FIGURE 19.14
RADARSAT-1 SAR intensity images of the Yukon River Basin, Alaska, acquired on (a) July 24, 2003, (b) August 17, 2003, (c) September 10, 2003, and (d) October 4, 2003. These SAR images show the progression of a fire that started in July 2003 (successively larger bright areas).

and inferring landscape changes based on InSAR coherence and SAR intensity imagery. Timely observations of precise land surface topography and time-transient surface changes will accelerate development of predictive models that can anticipate the effects of natural processes such as volcanic eruptions, earthquakes, landslides, and wildfires. With more and more operational SAR sensors available for timely data acquisitions, InSAR—coupled with state-of-the-art information technologies such as data-mining and grid computation—will continue to address and provide solutions to many scientific questions related to natural hazards monitoring and characterization in protected lands and elsewhere.

Acknowledgments

ERS-1/-2 and Envisat, RADARSAT-1, and JERS-1 SAR images are copyrighted © European Space Agency (ESA), Canadian Space Agency (CSA), and Japan

Aerospace Exploration Agency (JAXA), respectively. ALOS PALSAR data are copyrighted @ JAXA and Japan Ministry of Economy, Trade and Industry (METI). SAR data were provided by the Alaska Satellite Facility (ASF), JAXA, and ESA. The research summarized in this chapter was supported by funding from the NASA Earth Science & Interior Program and USGS Volcano Hazards Program. We thank many colleagues for their unselfish contributions to this research, and ASF, JAXA, and ESA staff members for their special efforts in making the SAR data available to us on a timely basis.

References

Baek, S., O. Kwoun, A. Braun, Z. Lu, and C.K. Shum. 2005. Digital elevation model of King Edward VII Peninsula, West Antarctica, from SAR interferometry and ICESat laser altimetry. *IEEE Geosci. Remote Sens. Lett.*, 2:413–417.

Bamler, R. and P. Hartl. 1998. Synthetic aperture radar interferometry. *Inverse Probl.*, 14:R1–54.

Berardino, P., G. Fornaro, R. Lanari, and E. Sansosti. 2002. A new algorithm for surface deformation monitoring based on small baseline differential SAR interferograms. *IEEE Trans. Geosci. Remote Sens.*, 40:2375–2383.

Bevis, M., S. Businger, T. Herring, C. Rocken, R. Anthes, and R. Ware. 1992. GPS meteorology: Remote sensing of the atmospheric water vapor using the Global Positioning System. *J. Geophys. Res.*, 97:15787–15801.

Biggs, J., R. Burgmann, J. Freymueller, Z. Lu, I. Ryder, B. Parsons, and T. Wright. 2009. The postseismic response to the 2002 M7.9 Denali Fault Earthquake: Constraints from InSAR. *Geophys. J. Int.*, 176:353–367.

Biggs, J., T. Wright, Z. Lu, and B. Parsons. 2007. Multi-interferogram method for measuring interseismic deformation: Denali Fault, Alaska. *Geophys. J. Int.*, 173:1165–1179.

Cervelli, P., M.H. Murray, P. Segall, Y. Aoki, and T. Kato. 2001. Estimating source parameters from deformation data, with an application to the March 1997 earthquake swarm of the Izu Peninsula, Japan. *J. Geophys. Res.*, 106:11,217–11,237.

Curlander, J. and R. McDonough. 1991. *Synthetic Aperture Radar Systems and Signal Processing* (New York: John Wiley & Sons).

Davis, P.M. 1986. Surface deformation due to inflation of an arbitrarily oriented triaxial ellipsoidal cavity in an elastic half-space, with reference to Kilauea Volcano, Hawaii. *J. Geophys. Res.*, 91:7429–7438.

Delaney, P.T. and D.F. McTigue. 1994. Volume of magma accumulation or withdrawal estimated from surface uplift or subsidence, with application to the 1960 collapse of Kilauea Volcano. *Bull. Volcanol.*, 56:417–424.

Dzurisin, D. 2007. *Volcano Deformation—Geodetic Monitoring Techniques* (Chichester, UK: Springer-Praxis Publishing Ltd).

Emardson, T.R., M. Simons, and F.H. Webb. 2003. Neutral atmospheric delay in interferometric synthetic aperture radar applications: Statistical description and mitigation. *J. Geophys. Res.*, 108:2231, doi:10.1029/2002JB001781.

Farr, T.G. et al. 2007. The shuttle radar topography mission. *Rev. Geophys.*, 45:RG2004, doi:10.1029/2005RG000183.

Ferretti, A., C. Prati, and F. Rocca. 1999. Multibaseline InSAR DEM Reconstruction: The wavelet approach. *IEEE Trans. Geosci. Remote Sens.*, 37:705–715.

Ferretti, A., C. Prati, and F. Rocca. 2001. Permanent scatterers in SAR interferometry. *IEEE Trans. Geosci. Remote Sens.*, 39:8–20.

Fialko, Y., Y. Khazan, and M. Simons. 2001. Deformation due to a pressurized horizontal circular crack in an elastic half-space, with applications to volcano geodesy. *Geophys. J. Int.*, 146:181–190.

Fialko, Y., D. Sandwell, D. Agnew, M. Simons, P. Shearer, and B. Minster. 2002. Deformation on nearby faults induced by the 1999 Hector Mine earthquake. *Science*, 297:1858–1862.

Fielding, E.J., M. Talebian, P.A. Rosen, H. Nazari, J.A. Jackson, M. Ghorashi, and R. Walker. 2005. Surface ruptures and building damage of the 2003 Bam, Iran, earthquake mapped by satellite synthetic aperture radar interferometric correlation. *J. Geophys. Res.*, 110:B03302, doi:10.1029/2004JB003299.

Foster, J. et al. 2006. Mitigating atmospheric noise for InSAR using a high-resolution weather model. *Geophy. Res. Lett.*, 33:L16304, doi:10.1029/2006GL026781.

Gray, A.L., K.E. Mattar, and G. Sofko. 2000. Influence of ionospheric electron density fluctuations on satellite radar interferometry. *Geophys. Res. Lett.*, 27: 1451–1454.

Gray, L. and P.J. Farris-Manning. 1993. Repeat-pass interferometry with airborne synthetic aperture radar. *IEEE Trans. Geosci. Remote Sens.*, 31:180–191.

Hanssen, R. 2001. *Radar Interferometry: Data Interpretation and Error Analysis* (Netherlands: Kluwer Academic Publishers).

Henderson F. and A. Lewis. 1998. *Principals and Applications of Imaging Radar—Manual of Remote Sensing* (John Wiley & Sons Inc.). **Q5**

Hensley S., R. Munjy, and P. Rosen. 2001. Interferometric synthetic aperture radar (IFSAR). In *Digital Elevation Model Technologies and Applications: The DEM Users Manual*, D.F. Maune (Ed.) (American Society for Photogrammetry and Remote Sensing). **Q6**

Hooper, A., P. Segall, and H. Zebker. 2007. Persistent scatterer interferometric synthetic aperture radar for crustal deformation analysis, with application to Volcán Alcedo, Galápagos. *J. Geophys. Res.*, 112:B07407, doi:10.1029/2006JB004763.

Jarlemark, P.O.J. and G. Elgered. 1998. Characterization of temporal variations in atmospheric water vapor. *IEEE Trans. Geosci. Remote Sens.*, 36:319–321.

Johnson, D. 1987. Elastic and inelastic magma storage at Kilauea volcano, Volcanism. In Hawaii, R. Decker, T. Wright, and P. Stauffer (Eds.). *USGS Professional Paper*, 1350:1297–1306.

Kwoun, O. and Z. Lu. 2009. Multi-temporal RADARSAT-1 and ERS backscattering signatures of coastal wetlands at southeastern Louisiana. *Photogramm. Eng. Remote Sens.*, 75:607–617.

Lee, C.W., Z. Lu, H.S. Jung, J.S. Won, and D. Dzurisin. 2010. Surface deformation of Augustine Volcano (Alaska), 1992–2005, from multiple-interferogram processing using a refined SBAS InSAR approach. USGS Professional Paper, in press. **Q7**

Levanon, N. 1988. *Radar Principles* (John Wiley & Sons). **Q8**

Li, F.K. and R.M. Goldstein. 1990. Studies of multibaseline spaceborne interferometric synthetic aperture radars. *IEEE Trans. Geosci. Remote Sens.*, 28:88–96.

Li, Z., J.-P. Muller, and P. Cross. 2003. Comparison of precipitable water vapor derived from radiosonde, GPS, and Moderate-Resolution Imaging Spectroradiometer measurements. *J. Geophys. Res.*, 108:4651, doi:10.1029/2003JD003372.

Li, Z., E. Fielding, P. Cross, and J.-P. Muller. 2005. InSAR atmospheric correction: GPS Topography-dependent Turbulence Model (GTTM). *J. Geophys. Res*. 110:B02404, doi:10.1029/2005JB003711.

Lu, Z. and J. Freymueller. 1998. Synthetic aperture radar interferometry coherence analysis over Katmai volcano group, Alaska. *J. Geophys. Res.*, 103:29887–29894.

Lu, Z., D. Mann, and J. Freymueller. 1998. Satellite radar interferometry measures deformation at Okmok volcano. *EOS Trans.*, 79:461–468.

Lu, Z., D. Mann, J. Freymueller, and D. Meyer. 2000. Synthetic aperture radar interferometry of Okmok volcano, Alaska: Radar observations. *J. Geophys. Res.*, 105: 10791–10806.

Lu, Z., E. Fielding, M. Patrick, and C. Trautwein. 2003a. Estimating lava volume by precision combination of multiple baseline spaceborne and airborne interferometric synthetic aperture radar: The 1997 eruption of Okmok Volcano, Alaska. *IEEE Trans. Geosci. Remote Sens.*, 41:1428–1436.

Lu, Z., T. Wright, and C. Wicks. 2003b. Deformation of the 2002 Denali Fault earthquakes, Alaska, mapped by RADARSAT-1 interferometry. *EOS Trans.*, 84: 425–431.

Lu, Z., T. Masterlark, and D. Dzurisin. 2005a. Interferometric synthetic aperture radar (InSAR) study of Okmok Volcano, Alaska, 1992–2003: Magma supply dynamics and post-emplacement lava flow deformation. *J. Geophys. Res.*, 110:B02403, doi:10.1029/2004JB003148.

Lu, Z., C. Wicks, O. Kwoun, J. Power, and D. Dzurisin. 2005b. Surface deformation associated with the March 1996 earthquake swarm at Akutan Island, Alaska, revealed by C-band ERS and L-band JERS radar interferometry. *Can. J. Remote Sens.*, 31(1):7–20.

Lu, Z. 2007. ALOS PALSAR InSAR. *NASA Alaska Satellite Facility News Notes*, 4(4):1–2.

Lu, Z. and O. Kwoun. 2008. RADARSAT-1 and ERS interferometric analysis over southeastern coastal Louisiana: Implication for mapping water-level changes beneath swamp forests. *IEEE Trans. Geosci. Remote Sens.*, 46:2167–2184.

Lu, Z. and D. Dzurisin. 2010. Ground surface deformation patterns, magma supply, and magma storage at Okmok volcano, Alaska, inferred from InSAR analysis: II. Co-eruptive deflation, July-August 2008. *J. Geophys. Res.*, 115:B00B02, doi:10.1029/2009JB006970.

Lu, Z., Dzurisin, D., Biggs, J., Wicks, C. Jr., and S. McNutt. 2010. Ground surface deformation patterns, magma supply, and magma storage at Okmok volcano, Alaska, from InSAR analysis: I. Inter-eruption deformation, 1997–2008. *J. Geophys. Res.*, 115:B00B03, doi:10.1029/2009JB006969.

Lu, Z., C. Wicks, D. Dzurisin, J. Power, S. Moran, and W. Thatcher. 2002. Magmatic inflation at a dormant stratovolcano: 1996–98 activity at mount Peulik Volcano, Alaska, revealed by satellite radar interferometry. *J. Geophys. Res.*, 107(B7):2134, doi:10.1029/2001JB000471.

Massonnet, D. and K. Feigl. 1998. Radar interferometry and its application to changes in the Earth's surface. *Rev. Geophys.* 36:441–500.

Meyer, F., R. Bamler, N. Jakowski, and T. Fritz. 2006. The potential of low-frequency SAR systems for mapping ionospheric TEC distributions. *IEEE Geosci. Remote Sens. Lett.*, 3:560–564.

Meyer, F. et al. 2010. A review of ionospheric effects in low-frequency SAR data. In **Q9** *International Geoscience and Remote Sensing Symposium* (abstract).

Mogi, K. 1958. Relations between the eruptions of various volcanoes and the deformations of the ground surface around them. *Bull. Earthquake Res. Inst. Univ. Tokyo*, 36:99–134.

Niell, A.E., A.J. Coster, F.S. Solheim, V.B. Mendes, P.C. Toor, R.B. Langley, and C.A. Upham. 2001. Comparison of measurements of Atmospheric Wet Delay by Radiosonde, Water Vapor Radiometer, GPS, and VLBI. *J. Atmos. Oceanic Technol.*, 18:830–850.

Okada, Y. 1985. Surface deformation due to shear and tensile faults in a half-space. *Bull. Seismol. Soc. Am.*, 75:1135–1154.

Press, W., S. Teukolsky, W. Vetterling, and B. Flannery. 1992. *Numerical Recipes in C, the Art of Scientific Computing*, (Cambridge: Cambridge University Press).

Ramsey, E. III, Z. Lu, A. Rangoonwala, and R. Rykhus. 2006. Multiple baseline radar interferometry applied to coastal landscape classification and changes. *GISci. Remote Sens.*, 43:283–309.

Rignot, E. and R. Thomas. 2002. Mass balance of polar ice sheets. *Science*, 297:1502–1506.

Rocca, F. 2007. Modeling interferogram stacks. *IEEE Trans. Geosci. Remote Sens.*, 45:3289–3299.

Rosen, P., S. Hensley, H. Zebker, F.H. Webb, and E.J. Fielding. 1996. Surface deformation and coherence measurements of Kilauea volcano, Hawaii, from SIR-C radar interferometry. *J. Geophys. Res.*, 101:23109–23125.

Rosen, P., S. Hensley, I.R. Joughin, F.K. Li, S.N. Madsen, E. Rodriguez, and R.M. Goldstein. 2000. Synthetic aperture radar interferometry. *Proc. IEEE*, 88:333–380.

Ruffino, G., A. Moccia, and S. Esposito. 1998. DEM generation by means of ERS tandem data. *IEEE Trans. Geosci. Remote Sens.*, 36:1905–1912.

Rykhus, R. and Z. Lu. 2010, Monitoring a 2003, Yukon Flats, Alaska wildfire using multi-temporal Radarsat-1 intensity and interferometric coherence images. *Geomatics Nat. Hazards Risk*, in press. **Q10**

Rykhus, R. and Z. Lu. 2007. Hurricane Katrina flooding and possible oil slicks mapped with satellite imagery. USGS Circular 1306: Science and the Storms—The USGS Response to the Hurricanes of 2005, pp. 50–53.

Sansosti, E. et al. 1999. Digital elevation model generation using ascending and descending ERS-1/ERS-2 tandem data. *Int. J. Remote Sens.*, 20:1527–1547.

Wegmuller, U., C. Werner, T. Strozzi, and A. Wiesmann. 2006. Ionospheric electron concentration effects on SAR and INSAR. In *International Geoscience and Remote Sensing Symposium*, Denver, Colorado, USA.

Wright, T. 2002. Remote monitoring of the earthquake cycle using satellite radar interferometry. *Phil. Trans. R. Soc. Lond.*, 360:2873–2888.

Zebker H. et al. 1992. The TOPSAR interferometric radar topographic mapping instrument. *IEEE Trans. Geosci. Remote Sens.*, 30:933–940.

Zebker, H.A. and J. Villasenor. 1992. Decorrelation in interferometric radar echoes. *IEEE Trans. Geosci. Remote Sens.*, 30:950–959.

Zebker, H.A., P.A. Rosen, R.M. Goldstein, A. Gabriel, and C.L. Werner. 1994. On the derivation of coseismic displacement fields using differential radar interferometry: The Landers earthquake. *J. Geophys. Res.*, 99:19617–19634.

Zebker, H., P. Rosen, and S. Hensley. 1997. Atmospheric effects in interferometric synthetic aperture radar surface deformation and topographic maps. *J. Geophys. Res.*, 102:7547–7563.

Cat #: K11949 **Chapter: 19**

TO: CORRESPONDING AUTHOR

AUTHOR QUERIES – TO BE ANSWERED BY THE AUTHOR

The following queries have arisen during the typesetting of your manuscript. Please answer these queries by marking the required corrections at the appropriate point in the text.

Query no.	Query	Response
Q1	Please check the shortened running head.	
Q2	Yang et al. (1988) is not listed in the reference list. Please provide complete publication details.	
Q3	Is the change in figure number to Figure 19.10 OK in 19.10i, 19.10l, 19.10m, 19.10n, and 19.10o.	
Q4	As figure set in gray scale. Please rephrase caption.	
Q5	Please provide place of publication in Henderson and Lewis (1998).	
Q6	Please provide place of publication in Hensley et al. (2001).	
Q7	Please update Lee et al. (2010) in the reference list and in the source line for Figure 19.8.	
Q8	Please provide place of publication in Levanon (1988).	
Q9	Please provide complete publication details of Meyer et al. (2010).	
Q10	Please update Rykhus and Lu (2010).	
Q11	Something is missing inside () in the caption for Figure 19.11a. Please check.	
Q12	As figure set in gray scale. Please rephrase caption.	